

Shearless edge transport barriers in L-H transition

L A Osorio^{1,2}, M Roberto³, I L Caldas¹, R L Viana⁴ and Y Elskens²

¹Universidade de São Paulo, Instituto de Física, São Paulo-SP, Brazil

²Aix-Marseille Université, UMR 7345 CNRS, Marseille, France

³Instituto Tecnológico da Aeronáutica, Departamento de Física, São José dos Campos-SP, Brazil

⁴Universidade Federal do Paraná, Departamento de Física, Curitiba-PR, Brazil

E-mail: laosorioq1@gmail.com

September 2022

Abstract. The L-H transition leads to a substantial reduction in transport levels in tokamaks and stellarators, improving the plasma confinement in such devices. After the transition, the plasma is in a high-confinement regime characterized by steep density and temperature gradients, with a large radial electric field at the plasma edge. In this paper, we show that, on using an $\mathbf{E} \times \mathbf{B}$ wave transport model on a test particle, such large electric fields can produce shearless transport barriers (STBs), which are related to the presence of non-monotonic sheared profiles, preventing almost all the chaotic flux at the plasma edge. The behavior of these barriers enables us to investigate the properties of the L-H transition as a function of the intensity of the electrostatic fluctuations and the depth of the typical radial electric field well-like profile, developed at plasma edge during the transition. We found that, as the radial electric field well depth increases, the shearless edge transport barrier becomes more resistant to perturbations and that, eventually, an improved plasma confinement regime is accessed. In this sense, we found results consistent with the experimental observations. In particular, the transition curve in the parameter plane associated with the STB has a fractal structure, thanks to the non-integrable nature of the associated Hamiltonian.

Keywords: L-H transition, radial electric field, $\mathbf{E} \times \mathbf{B}$ drift velocity, shearless transport barrier, chaotic transport

1. Introduction

The achievement of a regime of improved plasma confinement is one of the key elements of the scenarios proposed for a future thermonuclear reactor [1, 2]. A transition from a low-confinement (L-mode) to a high-confinement regime (H-mode) was first reported by [3] in the ASDEX tokamak, characterized by a strong reduction of the transport coefficients in the plasma edge, thanks to the formation of steep density and temperature gradients therein [3]. It is thought that the L-H transition, as it has been called, is caused by a large radial electric field at the plasma edge, as well as a fluctuation suppression by an $\mathbf{E} \times \mathbf{B}$ sheared poloidal rotation velocity [4, 5]. Such transition will occur when the level of turbulent fluctuations is large enough so that the Reynolds stress drive surpasses the damping of the $\mathbf{E} \times \mathbf{B}$ flow [6].

However, after 40 years of active research, the L-H transition still remains an open issue, and the question about the mechanism behind the strong radial electric field at the plasma edge is unsolved [7–11]. Yet, several experimental techniques have explored the L-H transition in a wide class of toroidal machines and, in particular, it has been shown that, in the L-H transition, the radial electric field develops a deep well-like structure inside the last closed flux surface (LCFS) [7, 12–15]. As the plasma confinement regime improves, the radial electric field well depth increases [7, 14].

In this paper, we show that the presence of strong radial electric fields in the plasma edge, which is a characteristic feature of the L-H transition, can cause the formation of a shearless transport barrier (STB) due to the presence of shearless tori. These STBs are basically invariant tori for which the rotation number has local extrema. Some works have shown that, when the plasma has non-monotonic sheared profiles for the electric and/or the magnetic fields, STBs appear [16–21]. So, in our numerical results, we indicate that the STBs can emerge typically when there is a thin well in the radial electric field profile at the plasma edge and, besides this, that the robustness of such barriers depends on the well depth.

Our results are obtained from a model of guiding center motion with $\mathbf{E} \times \mathbf{B}$ drift in tokamaks, in which we adopt non-monotonic profiles for the equilibrium radial electric field, and sheared profiles for both the safety factor and the plasma toroidal rotation [16]. Although

the spectrum of the turbulent electrostatic fluctuations is broadband, we simplify the model by taking only one spatial mode with a finite number of harmonics. This is already sufficient to demonstrate that the existence of well-like electric field profiles near the plasma edge is directly related to the onset of STBs in H-mode tokamak discharges.

Since the applied model has a Hamiltonian structure in an adequate Poincaré surface of section, the phase space flow generated by solving the equations of motion is area-preserving. If the plasma profiles were all monotonic, KAM theory would apply everywhere in phase space and shearless barriers would not be possible at all. However, since the profiles are non-monotonic, local extrema correspond to shearless invariant tori which act as dikes, preventing particle diffusion.

An undeniable advantage of simple models over large-scale computer simulations is the possibility of choosing a small number of system parameters to investigate the effects of their changes on the STB properties. The depth of the radial electric field well and the intensity of a single mode of the electrostatic potential perturbation can be varied in order to get a parameter plane indicating a transport property, namely, the mean escape time for particles. The frontier between escape and non-escape is fractal, which is ultimately the consequence of the complicated invariant curve structure of quasi-integrable Hamiltonian systems.

The remainder of this paper is organized as follows: Section 2 outlines the $\mathbf{E} \times \mathbf{B}$ drift wave transport model, whereas our numerical results on shearless edge transport barriers are presented in Section 3. The L-H transition, regarded from the point of view of our parameter plane, is discussed in Section 4. The last Section contains our conclusions.

2. $\mathbf{E} \times \mathbf{B}$ Drift Wave Transport Model

For a magnetically confined plasma in a tokamak, let us consider an individual test particle whose guiding center is moving along the magnetic field lines, $\mathbf{B}(\mathbf{x})$, with velocity $\mathbf{v}_{\parallel}(\mathbf{x})$ and drifted by a $\mathbf{v}_{\mathbf{E} \times \mathbf{B}}(t, \mathbf{x})$ velocity, such that

$$\frac{d\mathbf{x}}{dt} = v_{\parallel} \hat{b} + \mathbf{v}_{\mathbf{E} \times \mathbf{B}}, \quad \mathbf{v}_{\mathbf{E} \times \mathbf{B}} = \frac{\mathbf{E} \times \mathbf{B}}{B^2}, \quad (1)$$

where $\mathbf{x} = (r, \theta, \varphi)$ corresponds to the particle position

in toroidal coordinates, $v_{\parallel} = v_{\parallel}(\mathbf{x})$ is the plasma velocity component in the magnetic field direction, $\hat{b} = \mathbf{B}/B$, and $\mathbf{E} = \mathbf{E}(t, \mathbf{x})$ is the electric field experienced by the particle.

We assume, for simplicity, that the magnetic equilibrium surfaces cross sections are concentric circles and, therefore, that there is only a radial dependence of the plasma profiles. Also, we are ignoring the drifts due to the magnetic field lines curvature and magnetic gradients. To do that, some assumptions are made on the tokamak geometry and the magnetic field; mainly, we take the cylindrical approximation for the tokamak, for which $a/R = \varepsilon \ll 1$, with a and R the minor and major radius of the plasma, respectively, i.e. the plasma is treated as a $2\pi R$ periodic cylinder. Furthermore, we assume a screw pinch configuration such that $\mathbf{B}(r) = B_{\theta}\hat{e}_{\theta} + B_{\varphi}\hat{e}_{\varphi}$, with $B \approx B_{\varphi} \gg B_{\theta}$ and $B = \text{cst}$. The radial dependence of the magnetic field components will be determined through the safety factor profile, $q(r)$, as shown in (6) and figure 1(c).

The electric field, $\mathbf{E}(t, \mathbf{x})$, is considered as a rotation-free vector field, $\nabla \times \mathbf{E} = 0$. When this condition is fulfilled, the electric field can be called electrostatic, even with it depending explicitly on time. In the equilibrium, we are neglecting any contribution of the parallel electric field, \mathbf{E}_{\parallel} , and just consider the radial equilibrium part $E_r(r)\hat{e}_r$. Moreover, a perturbation is included through the electrostatic potential $\tilde{\phi}(t, \mathbf{x})$ and therefore

$$\mathbf{E}(t, \mathbf{x}) = E_r(r)\hat{e}_r - \nabla\tilde{\phi}(t, \mathbf{x}). \quad (2)$$

The floating electrostatic potential, $\tilde{\phi}(t, \mathbf{x})$, is written as a superposition of harmonic waves traveling in the poloidal and toroidal directions,

$$\tilde{\phi}(\theta, \varphi, t) = \sum_n \phi_n \cos(M\theta - L\varphi - n\omega_0 t - \alpha_n), \quad (3)$$

where M and L are their dominant wave numbers, respectively, ω_0 their fundamental angular frequency, ϕ_n the amplitude and α_n the phase for each perturbation mode.

In order to obtain (5), we adimensionalize (1) using the characteristic scales a , $E_a = |E_r(a)|$ and B according to

$$\begin{aligned} E'_r &= \frac{E_r}{E_a}, & \phi'_n &= \frac{\phi_n}{aE_a}, & v'_{\parallel} &= \frac{B}{E_a}v_{\parallel}, \\ t' &= \frac{E_a}{aB}t, & \omega'_0 &= \frac{aB}{E_a}\omega_0. \end{aligned} \quad (4)$$

On using two new variables, the action $I = (r/a)^2$ and the angle $\psi = M\theta - L\varphi$, the equation of

motion (1) reduces to the 1.5-degrees-of-freedom dynamical system

$$\begin{aligned} \frac{dI}{dt} &= 2M \sum_n \phi_n \sin(\psi - n\omega_0 t - \alpha_n), \\ \frac{d\psi}{dt} &= \varepsilon v_{\parallel}(I) \frac{[M - Lq(I)]}{q(I)} - \frac{M}{\sqrt{I}} E_r(I), \end{aligned} \quad (5)$$

where $q(I) = aI^{1/2}B/(RB_{\theta})$ is the safety factor radial profile. Also, as it is noted, the prime notation was omitted.

If $\phi_n = 0$ for all modes, I will remain constant and the dynamical system will be integrable. In this scenario, the guiding center of the test particle describes a helix of constant radius. Also, if $M \ll 1$, the variation of I could be neglected and the system treated as an integrable one. It means that, to have an effective perturbation propagating in the system, it is necessary to perturb the electric field along the poloidal direction with a perturbation wavelength smaller than 2π , since this will cause a radial $\mathbf{E} \times \mathbf{B}$ drift wave transport velocity.

The presented model, given by (5), was introduced in [16]. It considers robust shearless transport barriers which can appear when non-monotonic radial plasma profiles are regarded [16, 19, 22], e.g. for the equilibrium electric field, the plasma velocity or the safety factor. In this work, we investigate the influence of the equilibrium radial electric field profile on the chaotic transport when a tokamak operates in the L-mode and H-mode regimes. As we know, in the H-mode, close to the edge, a pedestal structure appears in the plasma density, pressure, and temperature profiles [3, 23, 24], which reflects in the typical well-like radial electric field profile [7, 25] and in the appearance of a transport barrier close to $I = 1$, i.e. close to the LCFS [26, 27].

In the next sections, we will show that, as the plasma changes from the L-mode to the H-mode, a shearless edge transport barrier can appear at plasma edge and that its robustness depends on the electric well depth, as it has been evidenced in several tokamaks worldwide [7, 13, 14, 25].

3. Shearless Edge Transport Barrier

We construct a numerical map integrating the dynamical system (5) and considering the solution at times $T_j = 2j\pi/\omega_0$, with $j = 0, 1, 2, 3, \dots, N$. This procedure defines a $\psi \times I$ stroboscopic Poincaré phase portrait, that, given an initial condition $\mathbf{P}_0 = (\psi_0, I_0)$, will describe the regular or the chaotic orbit $\Sigma_N = (\mathbf{P}_0, \mathbf{P}_1, \dots, \mathbf{P}_N)$. In this work, the results for the Poincaré sections were obtained using the well-known numerical integrator Runge-Kutta-Dormand-Prince of 8(7) order [28], with a tolerance of 10^{-13} .

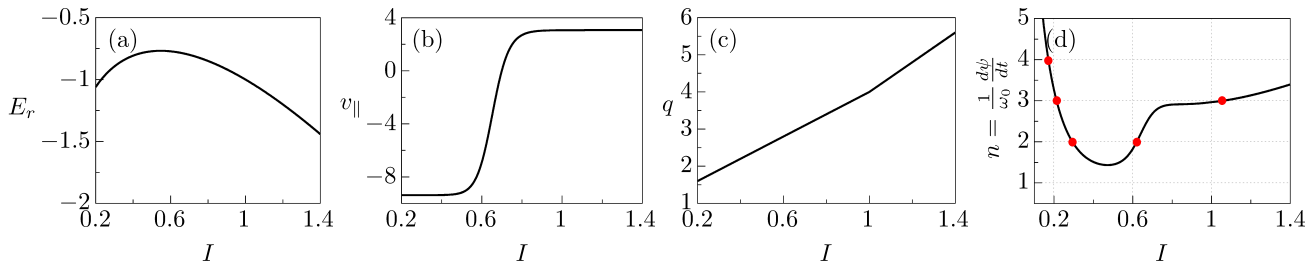


Figure 1. Plasma radial profiles for the (a) equilibrium radial electric field E_r , (b) toroidal plasma velocity v_{\parallel} , and (c) safety factor q . In panel (d), we show the resonance condition profile, indicating in red points the only resonant modes we are considering for the electrostatic perturbation potential, $n = 2, 3$ and 4 . The amplitude ϕ_1 , which is related with the non-resonant mode $n = 1$, is taken as one of the control parameters.

Additionally, we take into account the plasma profiles and parameters for the tokamak TCABR [19], mainly, the radial equilibrium electric field [19], $E_r(I)$, the plasma toroidal velocity [29], $v_{\parallel}(I)$, and the safety factor [30], $q(I)$, which are specified in (6) and in figure 1, respectively. For TCABR, the minor and major plasma radii are $a = 0.18$ m and $R = 0.61$ m, respectively, the tokamak minor radius $b = 0.21$ m and the toroidal magnetic field $B = 1.2$ T. Moreover, the characteristic scale of the electric field is taken as $E_a = 2.274$ kV/m. Explicitly,

$$\begin{aligned} E_r(I) &= 3\alpha I + 2\beta I^{1/2} + \gamma, \\ v_{\parallel}(I) &= \chi + \zeta \tanh(\xi I^{1/2} + \kappa), \\ q(I) &= \begin{cases} \rho + \zeta I & \text{if } I \leq 1 \\ (\rho + \zeta)I & \text{if } I > 1, \end{cases} \end{aligned} \quad (6)$$

where all the greek letters are dimensionless parameters which are kept fixed for the purpose of this work. They correspond to $\alpha = -1.14$, $\beta = 2.53$, $\gamma = -2.64$, $\chi = -3.16$, $\zeta = 6.22$, $\xi = 20.30$, $\kappa = -16.42$, $\rho = 1.00$ and $\varsigma = 3.00$.

In relation with the floating electrostatic potential parameters, based on the experimental data analysis made in [31], we take for the fundamental angular frequency $\omega_0 = 60$ rad \cdot kHz (approximately 5.70 rad after carrying out the adimensionalization), and as dominant spatial modes, $M = 16$ and $L = 3$. The phase constant is kept for all modes as $\alpha_n = \pi$.

The resonance conditions for the dynamical system (5) are given by

$$\begin{aligned} \frac{d}{dt}(\psi - n\omega_0 t - \alpha_n) &= 0, \\ \text{i.e. } n &= \frac{1}{\omega_0} \frac{d\psi}{dt}. \end{aligned} \quad (7)$$

When considering all the plasma profiles and parameters already defined above, we obtain the resonance conditions indicated in the profile of figure 1(d). Here, we mark with red dots the main resonant modes $n = 2, 3$ and 4 ; any contribution for $n > 4$ is neglected because they are near the plasma centre,

which is not in the scope of this work. So, from figure 1(d), we note that the modes $n = 2$ and $n = 3$ are resonant in two positions, while $n = 4$ just in one. The amplitudes of the electrostatic potential perturbation for each of these modes are taken as $\phi_2 = 8.0 \times 10^{-4}$ kV, $\phi_3 = 1.5 \times 10^{-3}$ kV and $\phi_4 = 8.5 \times 10^{-4}$ kV, which become the dimensionless fixed parameters 2.0×10^{-3} ,

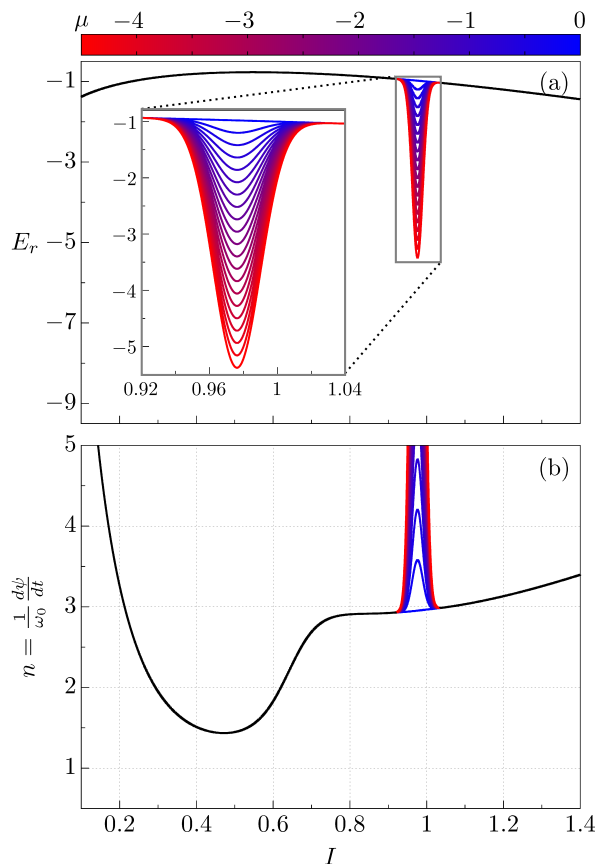


Figure 2. As we vary the control parameter μ , we see that close to the plasma edge a typical well-like electric field profile appears, figure (a). In part (b) of the figure, we see that the electric well can activate at plasma edge new resonant modes, directly related with the appearance of a shearless transport barrier.

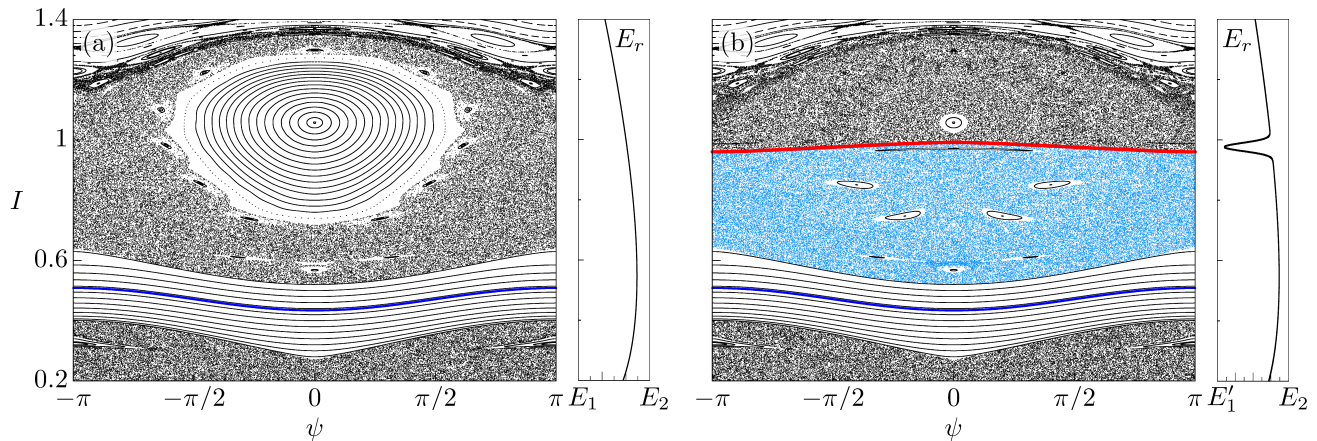


Figure 3. Poincaré sections for (a) $\phi_1 = 0.0$ and $\mu = 0.0$, and (b) $\phi_1 = 0.0$ and $\mu = -1.32$. To the right of each section, we show the radial equilibrium electric field profile used for the corresponding scenario. For (a), $E_1 = -2.0 < E_r(I) < E_2 = -0.5$, and for (b), $E'_1 = -2.5 < E_r(I) < E_2 = -0.5$. The shearless transport barriers are highlighted in blue (inner) and red (edge). Thus, we conclude that a pronounced electric shear with a shearless point at the plasma edge can onset an edge localized transport barrier.

3.7×10^{-3} , 2.1×10^{-3} , respectively.

In non-twist systems, STBs can appear and KAM theory does not apply [32, 33]. These barriers exhibit more resistance to perturbations than regular KAM tori, whose resistance is related with their rotation number, according to the KAM theorem [34]. Even

when a STB is broken up, a stickiness region can emerge preventing the chaotic flux [35, 36].

The existence of the STB can be associated with the extreme values of the rotation number profile, $\Omega(\psi_0, I_0)$, which is determined by (8), for a fixed initial value of ψ_0 :

$$\begin{aligned} \Omega(\psi_0, I_0) &= \lim_{N \rightarrow \infty} \frac{1}{2\pi} \frac{1}{N} \sum_{i=0}^{N-1} (\psi_{i+1} - \psi_i) \\ &= \lim_{N \rightarrow \infty} \frac{1}{2\pi} \frac{\psi_N(I_0) - \psi_0}{N}. \end{aligned} \quad (8)$$

Therefore, when $(d\Omega/dI_0)_{\mathbf{P}_{\text{STB}}} = 0$, the KAM assumption is violated and a shearless curve can be identified through the initial condition $\mathbf{P}_{\text{STB}} = (\psi_0, I_{\text{STB}})$.

In [19, 22], it was shown that non-resonant perturbation modes are able to break up or onset the STBs, even when the amplitude of the perturbation is increasing. In general, the barrier appears recurrently as the non-resonant amplitude of the perturbation varies. This reason leads us to regard ϕ_1 as one of the control parameters to study the chaotic transport at plasma edge.

First of all, let us consider the simplest scenario when $\phi_1 = 0$ and the electric field is the one in (6), see figure 3(a). In this case, we found a STB, marked in blue, using the rotation number profile shown by the black line from figures 4(a) and 4(b). But, even though there is a shearless transport barrier, a reasonable fraction of chaotic orbits above it are escaping and reaching the vessel wall, $I_{\text{wall}} = (b/a)^2 = 1.36$. Beyond this value, the trajectories lack physical sense; nevertheless, we plot the phase space just a little further. Also, the orbits trapped by the main island are crossing the LCFS.

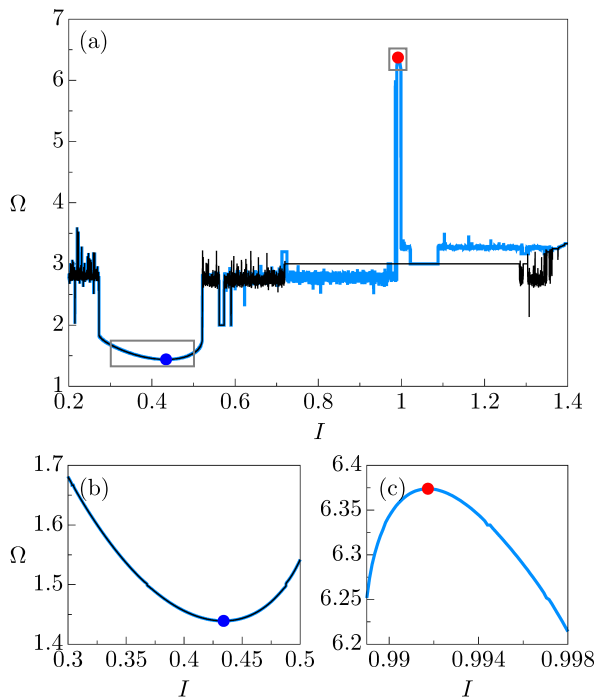


Figure 4. Rotation number profiles for $\phi_1 = 0.0$. (a) The black line holds for $\mu = 0.0$ and the blue one for $\mu = -1.32$. Parts (b) and (c) are magnifications of the rotation number profiles in part (a) related with the onset of a shearless transport barrier in the inner part and in the edge of the plasma, respectively. Here, $\psi_0 = 0$.

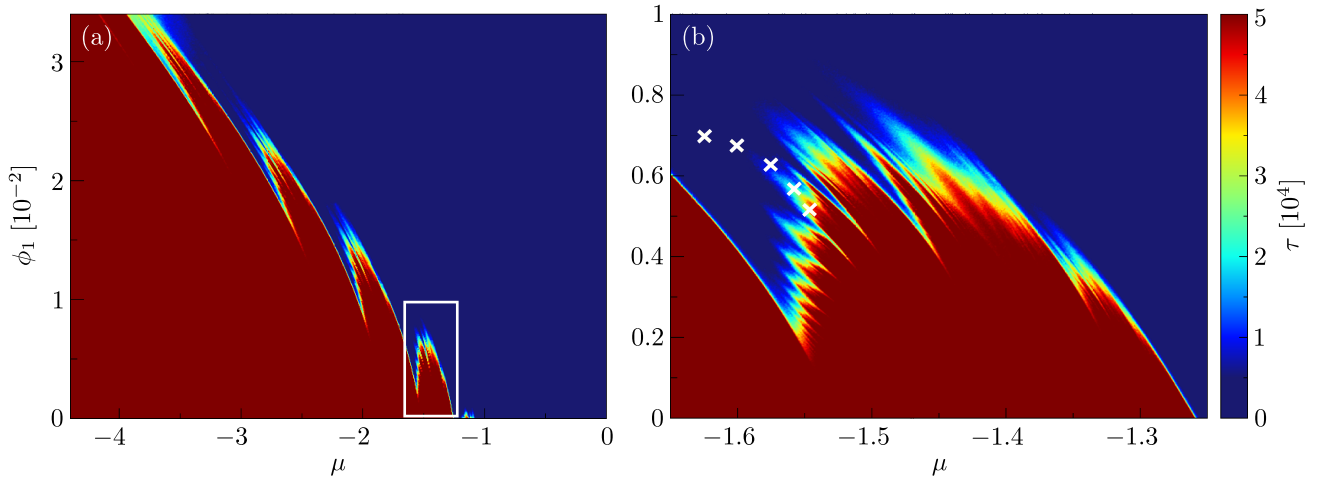


Figure 5. (a) Parameter space with the depth of the electric field well at plasma edge and the perturbation amplitude of the electrostatic potential of the non-resonant mode $n = 1$, $\mu \times \phi_1$. (b) Magnification inside the white rectangle in panel (a). The color bar indicates the mean escape time for an ensemble of initial conditions, calculated as shown in (10). The crosses in part (b) mark the pairs of parameters (μ, ϕ_1) used to get the next figure.

This confinement problem can be handled if we add, to our current E_r profile, a Low/High-mode-like electric field profile. Although this model does not consider any divertor and the magnetic equilibrium surfaces are circular, a H-mode confinement regime can be accessed by incorporating a biased electrode, which would be regarded as acting at the plasma edge, as it was experimentally observed in [37].

Then, let us assume a radial equilibrium electric field profile at plasma edge, $E_H(I)$, as the one given by

$$E_H(I) = \mu \exp \left[-\frac{1}{2} \left(\frac{\sqrt{I} - \delta}{\sigma} \right)^2 \right], \quad (9)$$

where $\delta = 0.988$ and $\sigma = 7 \times 10^{-3}$ are fixed dimensionless parameters which represent an estimation of the electric field well center position and its width.

The use of this expression to describe the L-mode and H-mode confinement regimes rests on the fact that it is easier to treat the most common parameters associated with L-H regimes, such as depth, width and well position. Moreover, it fits the experimental data [7, 15].

The well depth, $\mu \leq 0$, will be treated as a control parameter. Then, from figure 2, we observe that the inclusion of this kind of electric field profile, at plasma edge, will activate new resonant perturbation modes as its depth is increased. As a consequence, a new dynamics is induced close to $I = 1.0$, that, eventually, will provoke the onset of a new shearless curve.

For example, in figure 3(b), when $\mu = -1.32$, we show that an additional STB appears just before the plasma edge, confining almost all the chaotic flux

outside the plasma. So, the light-blue orbit cannot go through the red curve. To find this barrier, we calculated the rotation number profile shown by the blue line in figure 4(a) and (c). From these results, we observe that the presence of the new shearless edge transport barrier does not affect the dynamics closer to the plasma centre. We can see that even the inner invariant and the shearless curves still remain. This can be verified by looking at the rotation number behavior: the black and the blue lines, which correspond to the $\mu = 0.0$ and $\mu = -1.32$ cases, respectively, are indistinguishable at the beginning. It is just before $I = 0.6$ when we start to perceive the difference between the two scenarios.

In order to allow the edge transport barrier to appear, the main resonance needs to shrink. However, it is interesting to notice that, even then, the island conserves its rotation number. This is noticed looking at the rotation number profile just after $I = 1.0$, where both lines are superposed, figure 4(a).

A natural question still remains after observing the existence of the predicted barrier: does this barrier become more resistant as the depth of the electric field well radial profile at plasma edge increases? Experimental observations have shown that this actually happens, the main distinction between the radial equilibrium electric field profiles in L-mode, I-mode and H-mode is that the electric well is deeper as the confinement regime improves [7]. To answer that question, we surveyed the parameter space $\mu \times \phi_1$ to identify when the barrier can appear or be broken up.

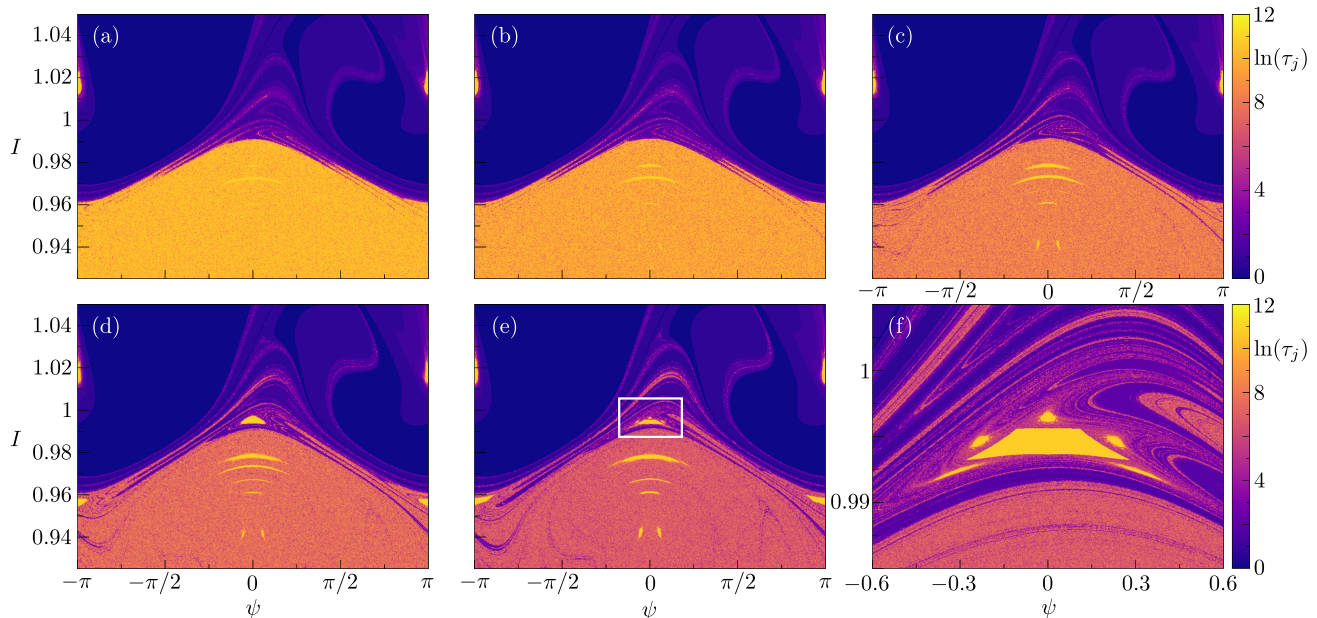


Figure 6. Escape time in phase space for (a) $\phi_1 = 5.25 \times 10^{-3}$ and $\mu = -1.55$, (b) $\phi_1 = 5.74 \times 10^{-3}$ and $\mu = -1.56$, (c) $\phi_1 = 6.35 \times 10^{-3}$ and $\mu = -1.58$, (d) $\phi_1 = 6.84 \times 10^{-3}$ and $\mu = -1.60$, and (e) $\phi_1 = 7.33 \times 10^{-3}$ and $\mu = -1.63$. Panel (f) corresponds to a magnification inside the white rectangle in panel (e).

4. L-H Transition

Non-resonant perturbation modes are able to break up or onset STBs, even when the amplitude of the perturbation is increasing [19, 22]. Also, a shearless edge transport barrier can appear when the equilibrium radial electric field profile exhibits a thin-well-like behavior at plasma edge.

Now, to study the resistance of the shearless edge transport barrier, we analyze the (μ, ϕ_1) parameters space. To do that, let us consider an ensemble of N_{IC} randomly chosen initial conditions in the chaotic region below the external barrier and iterate each of them a maximum of N_{max} crossings in the Poincaré section. We can establish a threshold, I_{up} , above the barrier and wait until the orbits reach it, then record the time, τ_j , they spent to get I_{up} ; for orbits which did not cross the barrier region, we kept the time as its maximum, N_{max} . With those times, we calculate the mean escape time

$$\tau = \frac{1}{N_{IC}} \sum_{j=1}^{N_{IC}} \tau_j. \quad (10)$$

To generate figures 5(a) and (b), we chose a 700×700 parameter space grid and we degraded the numerical integrator tolerance to 10^{-9} to limit the computational effort. We selected, for every pair (μ, ϕ_1) , $N_{IC} = 100$ randomly chosen initial condition in a line at $I_0 = 0.7$, and integrated them a maximum of $N_{max} = 5 \times 10^4$ to reach the threshold set up at $I_{up} = 1.05$.

For that, a parallel code was written using the MPI library, in which we take each pair (μ, ϕ_1) and run it in one of the available cores. This code was run using 352 cores from 11 nodes with processor Intel Xeon Gold 6142, which belong to the high performance computing resources of the Centre de Calcul Intensif d'Aix-Marseille. The computing time to get each of the figures 5(a) and (b) was about 1 week.

Now, when $\tau = N_{max}$, it means, from (10), that no particle escapes beyond the shearless edge transport barrier. On the other hand, when $\tau < N_{max}$, it means that there is not any barrier, but, in some cases, it could be a kind of resistance to the chaotic transport, e.g. a stickiness region.

In figure 5(a), we notice that, for values of μ between 0 and nearly -1.0 , no STB or opposition to the chaotic flux appear, no matter the amplitude of the perturbation. Then, around $\mu = -1.162$ the first barrier appears, but it is broken up for a small perturbation. As we move to the more negative values of μ , i.e. deeper electric field wells, the barrier gains resistance to the perturbation since it breaks up for larger amplitudes of ϕ_1 . It seems that we are accessing to improved regimes of confinement as the depth of the electric field well increases. After some value of μ , as we can see from the figure, the barrier does not break up. In some way, we are seeing an L-H transition through the description of shearless transport barriers, that, in general, maintain the same behavior as the experimental results already reported.

Besides, we notice that, for a fixed value of μ , the shearless barrier can appear and disappear recurrently, as it has been shown in [19, 22], and the same happens if we fix ϕ_1 , as we see clearly from the magnification shown in figure 5(b). This parameter space suggests that there is a fractal behavior, already discovered in other systems with shearless transport barriers, for example the standard non-twist map [38].

Also, it is interesting to notice that, every time when the barrier breaks up, a stickiness region appears, and it gets stronger for larger values of $|\mu|$. These stickiness regions are associated with large values of τ . But, even more interesting, the stickiness region covers a larger area of the parameter space when we are in a fractal-like boundary. When we are close to a regular boundary, the area covered by the stickiness is smaller and the stickiness ends easily.

To extend our study of what is happening after the barrier breaks up, we plotted the escape time, τ_j , for a 700×700 grid of initial conditions close to the plasma edge in phase space, see figure 6. The control parameters we chose for this analysis are marked in figure 5(b). In part (a) of figure 6, we notice that, after the barrier breaks up, a big resistance to the chaotic flux appears; the orbits spend a large time to cross the edge. This is due to there being few chaotic routes that can be taken, which, as we can see from the figure, are concentrated at $\psi = 0$. The scenario in part (b) is not very different from the previous one, however, the escape time is a little smaller. In part (c) of the figure, fast routes enter inside the chaotic region and, in part (d), a period-two island chain emerges. In part (e), these islands are surrounded by secondary ones, and these ones by others even smaller, and so on. The global behavior, as we see in figure (f), is that the presence of these island allows the onset of many fast routes, probably in a fractal way, through the plasma edge.

5. Conclusions

The transition between a low and a high plasma confinement regime has been intensively studied since it was experimentally observed in tokamak discharges. In this paper, we showed that, during an LH-transition, there appears a shearless transport barrier close the LCFS which may contribute to the decrease of the particle and heat radial fluxes, so improving the quality of plasma confinement. These shearless transport barriers have been described by using a transport model for $\mathbf{E} \times \mathbf{B}$ drift in magnetized plasmas, considering the electric field as the result of: (i) an equilibrium radial part with non-monotonic profile, and (ii) a perturbation part caused by electrostatic fluctuations propagating along the

poloidal and toroidal directions. In our model, we also considered radial profiles for the safety factors of the equilibrium magnetic surfaces and the toroidal plasma velocity. The numerical simulations we presented in this paper were obtained using parameter values taken from the TCABR tokamak, but the results are valid for a wide class of toroidal machines.

The combination of the velocity, electric, and magnetic field plasma profiles leads to a non-monotonic behavior in the rotation number radial profile. Shearless transport barriers occur at those positions for which this rotation number has local extrema, i.e. where there is no shear at all. There were considered three resonant and one non-resonant electrostatic waves, but, for simplicity, we have chosen only the non-resonant mode amplitude as control parameter. The latter was varied in order to investigate the role of the perturbation strength on the properties of the shearless barrier. In particular, we showed that, on varying this non-resonant mode amplitude, shearless barriers can appear or disappear in a recurrent way.

As a numerical diagnostic of the existence of the shearless barrier, we computed the average escape time it takes for a set of guiding-center orbits to achieve a given threshold above the barrier location. If this escape time reaches its maximum value, we say that, up to the numerical accuracy, the shearless barrier exists. The appearance and disappearance of barriers were found to depend on the control parameter in an intermittent fashion. Moreover, this technique also allowed us to characterize regions of sticky behavior, occurring when the particle spends a long time near some resonance before escaping away through a chaotic orbit. We found that stickiness behavior exists before the appearance of a shearless barrier and after its disappearance, no matter how small is the transition interval considered.

We also implemented a new electric field radial profile with a well-like structure localized near the plasma edge. By doing this, we were able to impose new resonance conditions close the LCFS and, therefore, a new dynamics therein that derives in the onset of a shearless curve close the plasma edge, which reinforces the role of the electric field well in the LH transition. The well depth was chosen as the second control parameter used in our numerical simulations. Analogously to the former case, we studied the appearance/disappearance of the shearless edge barrier using the average escape time. Together with the first control parameter (the mode amplitude) we obtained a two-dimensional parameter space, in which we locate the fractal curves indicating the LH transition as well as the existence of stickiness regions.

One of our key results is that the shearless edge barrier becomes more robust as the well depth

increases, in accordance with experimental results. Therefore, the deeper is the electric profile well (i.e. the more pronounced is the electric field shear), the larger has to be the perturbation strength (caused by the non-resonant mode amplitude) in order to break up the shearless barrier and have an effective chaotic transport at the plasma edge. Moreover, just after the shearless barrier breakdown, the stickiness behavior causes the escape time to be so large that the confinement time of the plasma can still be satisfactory. However, in other regions of the parameter space we have typically small escape times, causing a significative decrease in the plasma confinement time.

Acknowledgments

The authors thank the financial support from the Brazilian Federal Agencies (CNPq), grants 407299/2018-1 and 302665/2017-0, the São Paulo Research Foundation (FAPESP, Brazil) under grants 2018/03211-6, 2018/14435-2 and 2020/01399-8, the Coordenação de Aperfeiçoamento de Pessoal de Nível Superior (CAPES) under Grant Nos. 88881.143103/2017-01 and 88887.675569/2022-00, and the Comité Français d'Evaluation de la Coopération Universitaire et Scientifique avec le Brésil (COFECUB) under Grant No. 40273QA-Ph908/18.

The Centre de Calcul Intensif d'Aix-Marseille is acknowledged for granting access to its high performance computing resources.

References

- [1] Wagner F 2007 *Plasma Physics and Controlled Fusion* **49** B1
- [2] Staebler A, Sips A, Brambilla M, Bilato R, Dux R, Gruber O, Hobirk J, Horton L, Maggi C, Manini A *et al.* 2005 *Nuclear fusion* **45** 617
- [3] Wagner F, Becker G, Behringer K, Campbell D, Eberhagen A, Engelhardt W, Fussmann G, Gehre O, Gernhardt J, Gierke G *et al.* 1982 *Physical Review Letters* **49** 1408
- [4] Biglari H, Diamond P and Terry P 1990 *Physics of Fluids B: Plasma Physics* **2** 1
- [5] Burrell K 1997 *Physics of Plasmas* **4** 1499
- [6] Diamond P, Liang Y M, Carreras B and Terry P 1994 *Physical review letters* **72** 2565
- [7] Viezzer E, Pütterich T, Conway G, Dux R, Happel T, Fuchs J, McDermott R, Ryter F, Sieglin B, Suttrop W *et al.* 2013 *Nuclear Fusion* **53** 053005
- [8] Hassam A, Antonsen Jr T, Drake J and Liu C 1991 *Physical review letters* **66** 309
- [9] Heikkinen J, Kiviniemi T and Peeters A 2000 *Physical review letters* **84** 487
- [10] Shaing K C and Crume Jr E 1989 *Physical Review Letters* **63** 2369
- [11] Itoh S I and Itoh K 1989 *Nuclear fusion* **29** 1031
- [12] Gohil P, Burrell K and Carlstrom T 1998 *Nuclear fusion* **38** 93
- [13] Burrell K, West W, Doyle E, Austin M, DeGrassie J, Gohil P, Greenfield C, Groebner R, Jayakumar R, Kaplan D *et al.* 2004 *Plasma physics and controlled fusion* **46** A165
- [14] McDermott R, Lipschultz B, Hughes J, Catto P, Hubbard A, Hutchinson I, Granetz R, Greenwald M, LaBombard B, Marr K *et al.* 2009 *Physics of Plasmas* **16** 056103
- [15] Sauter P, Pütterich T, Ryter F, Viezzer E, Wolfrum E, Conway G, Fischer R, Kurzan B, McDermott R, Rathgeber S *et al.* 2011 *Nuclear Fusion* **52** 012001
- [16] Horton W, Park H B, Kwon J M, Strozzi D, Morrison P and Choi D I 1998 *Physics of Plasmas* **5** 3910
- [17] Caldas I L, Viana R L, Szezech Jr J, Portela J S E, Fonseca J, Roberto M, Martins C G L and Da Silva E 2012 *Communications in Nonlinear Science and Numerical Simulation* **17** 2021
- [18] del Castillo-Negrete D and Martinell J 2012 *Communications in Nonlinear Science and Numerical Simulation* **17** 2031
- [19] Marcus F A, Roberto M, Caldas I L, Rosalem K and Elskens Y 2019 *Physics of Plasmas* **26** 022302
- [20] Grime G, Roberto M, Caldas I, Viana R and Elskens Y 2022 *arXiv preprint arXiv:2207.02823*
- [21] Morrison P J 2000 *Physics of Plasmas* **7** 2279
- [22] Osorio L A, Roberto M, Caldas I L, Viana R L and Elskens Y 2021 *Physics of Plasmas* **28** 082305
- [23] Connor J and Wilson H 2000 *Plasma physics and controlled fusion* **42** R1
- [24] ASDEX Team 1989 *Nuclear Fusion* **29** 1959
- [25] Ida K, Hidekuma S, Miura Y, Fujita T, Mori M, Hoshino K, Suzuki N and Yamauchi T (JFT-2M Group) 1990 *Phys. Rev. Lett.* **65** 1364
- [26] Wagner F, Fussmann G, Grave T, Keilhacker M, Kornherr M, Lackner K, McCormick K, Müller E, Stäbler A, Becker G *et al.* 1984 *Physical Review Letters* **53** 1453
- [27] Horton L, Chankin A, Chen Y, Conway G, Coster D, Eich T, Kaveeva E, Konz C, Kurzan B, Neuhauser J *et al.* 2005 *Nuclear fusion* **45** 856
- [28] Prince P J and Dormand J R 1981 *Journal of computational and applied mathematics* **7** 67
- [29] Severo J, Nascimento I C, Tsy-pin V and Galvão R M O 2003 *Nuclear fusion* **43** 1047
- [30] Fernandes T 2016 *Instabilidades MHD no tokamak TCABR* Master's thesis Universidade de São Paulo
- [31] Grenfell G G 2016 *Estudo de efeitos da polarização eletrostática periférica no Tokamak TCABR* Master's thesis Universidade de São Paulo
- [32] del Castillo-Negrete D and Morrison P 1993 *Physics of Fluids A: Fluid Dynamics* **5** 948
- [33] del Castillo-Negrete D, Greene J and Morrison P 1996 *Physica D: Nonlinear Phenomena* **91** 1
- [34] Reichl L E 1992 *The Transition to Chaos In Conservative Classical Systems : Quantum Manifestations* (Berlin: Springer-Verlag)
- [35] Szezech Jr J, Caldas I L, Lopes S R, Morrison P and Viana R L 2012 *Physical Review E* **86** 036206
- [36] Szezech Jr J, Caldas I, Lopes S, Viana R and Morrison P 2009 *Chaos: An Interdisciplinary Journal of Nonlinear Science* **19** 043108
- [37] Grenfell G G, Nascimento I, Oliveira D, Guimarães-Filho Z, Elizondo J, Reis A, Galvão R, Baquero W, Oliveira A, Ronchi G *et al.* 2018 *Physics of Plasmas* **25** 072301
- [38] Mathias A, Mugnaine M, Santos M, Szezech Jr J D, Caldas I L and Viana R L 2019 *Physical Review E* **100** 052207